RSC Advances

PAPER

View Article Online
View Journal | View Issue

Cite this: *RSC Adv.*, 2026, **16**, 3152

Sustainable synthesis of biocompatible nano-hydroxyapatite from seashell (micro-mollusk) waste

Mashrafi Bin Mobarak, *[a] Md Sohag Hossain, [ab] Aima Tanjim Khan, [c] Fariha Chowdhury *[d] and Samina Ahmed *[a]

Herein, we report a simple and sustainable wet chemical synthesis of nano-hydroxyapatite (nHAp) from micro-mollusk (seashell) waste collected from Saint Martin's Island, Bangladesh. The collected micro-mollusk contained around 96.7% of CaO measured by Wavelength Dispersive X-ray Fluorescence (WDXRF) spectroscopy. X-ray Diffraction (XRD) pattern of the synthesized nHAp matched with the ICDD standard data and confirmed the hexagonal HAp with nanocrystalline peaks. Crystallite size was estimated by exploiting multiple methods where the size ranged from around 2.6–16.5 nm. The nano-sized nature along with the morphology was confirmed through Field Emission Scanning Electron Microscope (FESEM) and Transmission Electron Microscope (TEM) analysis, where the particle sizes were measured to be 32.11 ± 11.38 nm (N = 105) and 14.95 ± 5.37 nm (N = 33), respectively. Fourier Transform Infrared Spectroscopy (FTIR) and Raman Spectroscopy were employed to confirm the existing functional groups, primarily the vibrational modes of PO_4^{3-} groups. They also confirmed the presence of B-type carbonate substitution of the synthesized nHAp. X-ray Photoelectron Spectroscopy (XPS) analysis was carried out to confirm the surface elemental composition (Ca, P, O and C), along with Na which was not detected in EDX analysis. Simultaneous Thermal Analysis (STA) indicated a total mass loss of 7.7% up to 597.5 °C and high thermal stability. The specific surface area was measured to be 72.98 m^2 g^{-1} by Brunauer–Emmett–Teller sorptometer (BET) analysis. The *in vitro* cell viability assay showed >95% cell viability at 100 μg mL^{-1}. The results demonstrate the successful synthesis of nHAp by utilizing micro-mollusk waste, which is biocompatible and suitable for biomedical and environmental applications.

Received 28th November 2025
Accepted 29th December 2025

DOI: 10.1039/d5ra09194b

rsc.li/rsc-advances

1. Introduction

Hydroxyapatite (HAp), with the chemical formula $Ca_{10}(PO_4)_6(OH)_2$ is a naturally occurring calcium phosphate mineral. This mineral is the primary inorganic component of human bones and teeth. It accounts for approximately 65–70% of bone by weight and about 97% of tooth enamel.[1] Structurally, HAp features a hexagonal crystal lattice with space group $P6_3/m$ and the typical lattice parameters are $a = b \approx 9.42$ Å and $c \approx 6.88$ Å. The structural feature of HAp enables ionic substitutions such as carbonate and fluoride that influence its bioresorbability as well as mechanical properties.[2] Some of the key attributes of HAp include outstanding biocompatibility, osteoconductivity, bioactivity, and thermal stability, which makes it non-toxic and supportive of bone regeneration without adverse immune responses.[3] These properties allow its extensive applications in biomedicine, including bone grafts, dental implants, and orthopedic coatings that promote osseointegration.[4] Additionally, HAp also has applications in drug delivery systems for therapeutics like antibiotics, environmental remediation and as a catalyst in chemical synthesis. As a biomimetic material, HAp integrates well with host tissue and is widely used in regenerative medicine and tissue engineering.[5]

Generally, HAp synthesis methods such as wet chemical precipitation, sol–gel, hydrothermal, or solid-state synthesis methods utilize precursors like calcium nitrate and di-ammonium phosphate to precisely control the stoichiometry and morphology.[6] However, these techniques often require high costs, substantial energy demands, and environmental drawbacks from the chemical reagents and waste generation.[7] In response, sustainable approaches are widely exploited as they utilize natural waste sources for extraction that enables circular economy goals by repurposing calcium rich wastes into value added materials.[8] Eggshells contains around 94–97% of $CaCO_3$

[a]*Institute of Glass and Ceramic Research and Testing (IGCRT), Bangladesh Council of Scientific and Industrial Research (BCSIR), Dhaka-1205, Bangladesh. E-mail: mashrafibinmobarak@gmail.com; shanta_samina@yahoo.com*

[b]*Department of Chemistry, Louisiana State University, Baton Rouge, Louisiana 70803, USA*

[c]*Department of Chemistry, Gopalganj Science and Technology University, Gopalganj – 8105, Bangladesh*

[d]*Biomedical and Toxicological Research Institute (BTRI), Bangladesh Council of Scientific and Industrial Research (BCSIR), Dhaka-1205, Bangladesh. E-mail: chowdhuryfariha@gmail.com*

which can be transformed into biocompatible nano-HAp through reacting with phosphate precursor.[3,9] Similarly, fish scales, bones, and seashells can also be used for HAp preparation and the present trace elements such as magnesium enhances the bioactivity.[10] Seashells with 95–99% of $CaCO_3$ have emerged as a prime feedstock of HAp due to their high calcium content as well as the presence of trace elements.[11] A myriad of studies have reported the utilization of seashells for HAp synthesis.[12–15]

Seashells are calcareous exoskeletons secreted by marine mollusks, predominantly composed of $CaCO_3$ polymorphs (calcite or aragonite) in layered architectures with organic matrices like conchiolin for resilience. They are classified into bivalves (two hinged shells like clams and oysters), gastropods (single, often spiraled shells like snails), and cephalopods (which have an external or internal shell like the nautilus).[16] Exploitation of seashells for HAp synthesis is convincing as global aquaculture generates over 10 million tons of mollusk shells waste annually.[17] These wastes enable a renewable, low-cost calcium reservoir. Micro-mollusks, are mollusks with adult shells <5 mm that comprises diminutive gastropods and bivalves forming dense intertidal deposits.[18,19] Their aragonite-rich shells, abundant on tropical shores like Bangladesh's Cox's Bazar, enable facile milling into fine precursors or can be direct calcined to form CaO, allowing the synthesis of nHAp. Utilizing micro-mollusks restricts overlooked waste, nurtures localized sustainability, and unlocks a new source for biomaterial synthesis.

Herein, for the first time to the best of our knowledge, reporting the synthesis of nHAp from micro-mollusks sourced from Saint Martin's Island, Bangladesh by employing a wet chemical route. Comprehensive characterization *via* XRD, FTIR, Raman, FESEM-EDS, TEM, XPS, STA, and BET unveiled the crystalline phase, existing functional groups, morphology, particle size, surface chemistry, thermal stability and surface area. This inaugural use of micro-mollusks as precursors contributed to the innovative and sustainable HAp production.

2. Materials and methods

2.1. Materials

Micro-mollusks (seashells) were obtained from the shores of Saint Martin's Island, Cox's Bazar, Chittagong, Bangladesh (20° 37′47.6″N 92°18′56.6″E). Samples were collected at low tide, where dense deposits of micro-mollusks form on the shore. The chemicals used for the synthesis were phosphoric acid (H_3PO_4, 85% purity, CAS: 7664-38-2), and ammonia solution (NH_4OH; CAS: 1336-21-6) which were procured from Merck KGaA, Germany, and sourced Scharlau, Spain. De-ionized (DI) water was used to make all the solutions and rinsing purposes.

2.2. Methods

2.2.1. Processing of micro-mollusks. The micro-mollusks were first washed with running tap water to remove dirt and sand particles. The shells were then sundried for a few hours and sieved through 20 mesh size (<850 μm) to separate chunks of large corals and other undesired materials. Around 17 g of the dried and sorted micro-mollusks were then weighed and subjected to ball milling at 450 rpm with ball: sample ratio of 10 : 1 for 1 hour. The milled powders were then analyzed with WDXRF in order to detect the present elements, as well as their quantity. Results are presented in Table 1.

2.2.2. Preparation of nHAp from micro-mollusks. Around 10 g of micro-mollusk powder was subjected to calcination at 900 °C which was achieved at a 10 °C min^{-1} heating rate, stayed for 2 hours and cooled to room temperature naturally. This procedure converted the $CaCO_3$ component present in micro-mollusk into CaO.[8] From this freshly prepared CaO powder, 5.6 g was weighed, mixed with 100 mL DI water and stirred for an hour to convert the CaO into $Ca(OH)_2$. Maintaining a Ca/P ratio of 1.67, 100 mL of 0.6 M H_3PO_4 solution was added dropwise under constant stirring. As the H_3PO_4 was added, white precipitate of calcium phosphate started to from. Once the H_3PO_4 solution was completely added, the solution mixture was stirred for another 30 minutes, followed by pH adjustment to ~11 by dropwise addition of ammonia solution. After pH adjustment, the mixture was stirred for 4 hours and then left undisturbed overnight for aging or crystal growth purposes. Afterwards, vacuum filtration was carried out to separate the nHAp from the supernatant, followed by drying in an oven at 105 °C for several hours. The dried nHAp chunks were ground in a mortar and pestle to make powder consistency and stored in air-tight conditions for further use. This synthesis scheme has been presented in Fig. 1.

2.2.3. Characterization of synthesized nHAp. The synthesized HAp from micro-mollusks were characterized by the following techniques: X-ray diffractometry (XRD, Panalytical Empyrean EMP3), Fourier-transform infrared spectroscopy (FTIR, Shimadzu IR Prestige21 – MIRacle10 ATR accessory), Raman spectroscopy (Horiba MacroRam, 785 nm diode laser), field emission scanning electron microscopy (FESEM) – energy dispersive X-ray spectroscopy (EDS) (JEOL JSM-7610F), transmission electron microscopy (TEM, Talos F200X G2), X-ray photoelectron spectroscopy (XPS, Thermo Scientific K-ALPHA),

Table 1 WDXRF result of micro-mollusk powder sample

Component	Result (mass%)	Line	Intensity
Na_2O	0.769	Na-Kα	1.1207
MgO	0.207	Mg-Kα	0.8511
Al_2O_3	0.243	Al-Kα	4.1187
SiO_2	0.594	Si-Kα	9.9773
P_2O_5	0.0325	P-Kα	1.1995
SO_3	0.222	S-Kα	6.5696
Cl	0.0610	Cl-Kα	1.2101
K_2O	0.0490	K-Kα	1.0556
CaO	96.7	Ca-Kα	1283.4375
MnO	0.0395	Mn-Kα	0.3112
Fe_2O_3	0.275	Fe-Kα	3.2231
ZnO	0.0325	Zn-Kα	1.6655
Br	0.0051	Br-Kα	0.7756
SrO	0.664	Sr-Kα	127.7762
Y_2O_3	0.0092	Y-Kα	1.9465
ZrO_2	0.135	Zr-Kβ1	6.9455

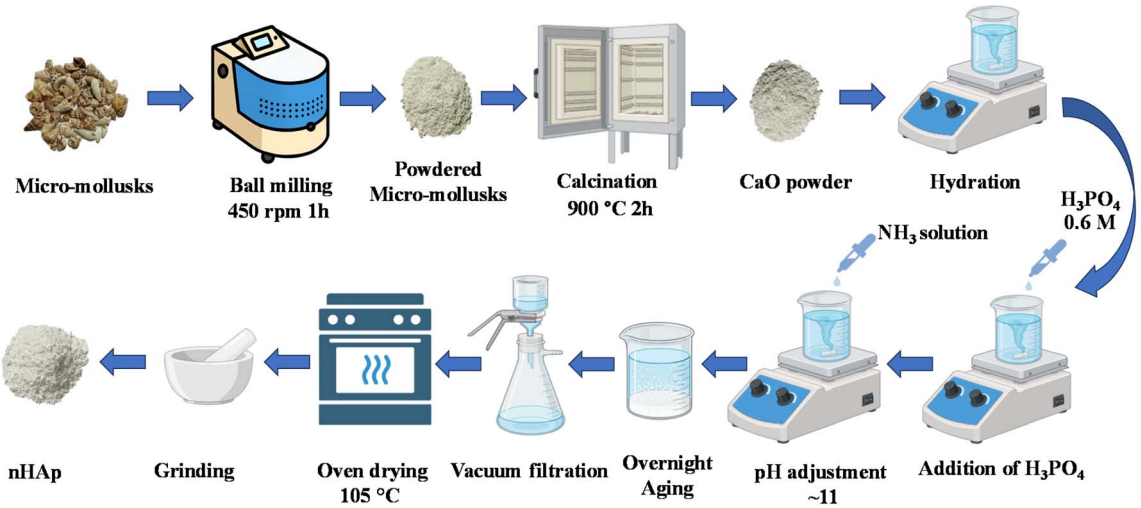

Fig. 1 Graphical illustration of nHAp from micro-mollusks by simple wet chemical precipitation method.

wavelength dispersive X-ray fluorescence (WDXRF, Bruker S8 TIGER), simultaneous thermal analyzer (STA, NETZSCH STA 449 F5), Brunauer–Emmett–Teller sorptometer (BET-201-A, PMI, Tampa, FL, USA).

2.2.4. Cell viability assay. The procedure for cell viability assay can be found in our previous studies.[20,21] Briefly, the Vero cell lines, which are kidney epithelial cells derived from the African green monkey (sourced from ThermoFisher Scientific, UK) was cultured in Dulbecco's Modified Eagle Medium (DMEM) supplemented with 1% penicillin-streptomycin (1 : 1 mixture), 0.2% gentamycin, and 10% fetal bovine serum (FBS). Cells at a density of 1.5×10^4 per 100 μL were seeded into 96-well plates and incubated for 24 hours at 37 °C in a 5% CO_2 atmosphere (Nuaire, USA). Following incubation, 25 μL of the HAp sample was introduced into each well, and the cyto-compatibility was assessed after another 24 hours incubation. Observations were made under a trinocular microscope (Optika, Italy), and cell counts were determined using an automated hemocytometer. All tests were performed in duplicate. Cell viability was then calculated using the following equation.

$$\text{Cell viability} = \frac{\text{number of live cells}}{\text{total number of cells}} \times 100\% \quad (1)$$

3. Results and discussion

3.1. X-ray diffraction (XRD) study

XRD analysis was carried out to confirm the formation of nHAp phase from the micro-mollusks. Fig. 2a shows the XRD pattern where multiple distinct and sharp diffraction peaks are clearly evident. The "search and match" operation through the X'pert Highscore software confirmed the formation of nHAp by closely matching it with the ICDD (International Centre for Diffraction Data) card #96-900-2215.[22] The peaks are well-defined and contain noticeable broadening. This broadening suggests the presence of nano-crystallinity. The sharpest peak was observed at around 31.88° which corresponds to the (211) plane. The other observed sharp peaks are 25.93° (002), 28.39° (102), 33.99° (202), 39.67° (310), 46.57° (222), 49.4° (213), 53.18° (004), and 64.08° (233), which are all indicative of typical nHAp's hexagonal crystal structure (space group $P6_3/m$, space group number 176).[23,24]

The XRD data was used to calculate different crystallographic parameters of the synthesized nHAp. For instance, the lattice parameters, volume and density of unit cell, crystallite size (though Scherrer's method), micro-strain, dislocation density and degree of crystallinity of the prepared nHAp were calculated based on eqn (2)–(8), respectively.[25,26]

$$\frac{1}{d^2} = \frac{4}{3}\left(\frac{h^2 + hk + k^2}{a^2}\right) + \frac{l^2}{c^2} \quad (2)$$

$$V = \frac{\sqrt{3}}{2}a^2c \quad (3)$$

$$\rho = \frac{zM}{N_A V} \quad (4)$$

$$D = \frac{k\lambda}{\beta \cos\theta} \quad (5)$$

$$\varepsilon = \frac{\beta}{4 \tan\theta} \quad (6)$$

$$\delta = \frac{1}{D^2} \quad (7)$$

$$X_c = \left(\frac{K_a}{\beta_{(211)}}\right)^3 \quad (8)$$

Here, eqn (2) represents the lattice parameter equation for hexagonal nHAp structure where, d = d-spacings, a, b, c = lengths of unit cell and h, k, l = miller indices. Eqn (3) and **(4)** represents the volume (V) and density (ρ) of the unit cell, where z = no. of formula unit per unit cell, M = molar mass, N_A =

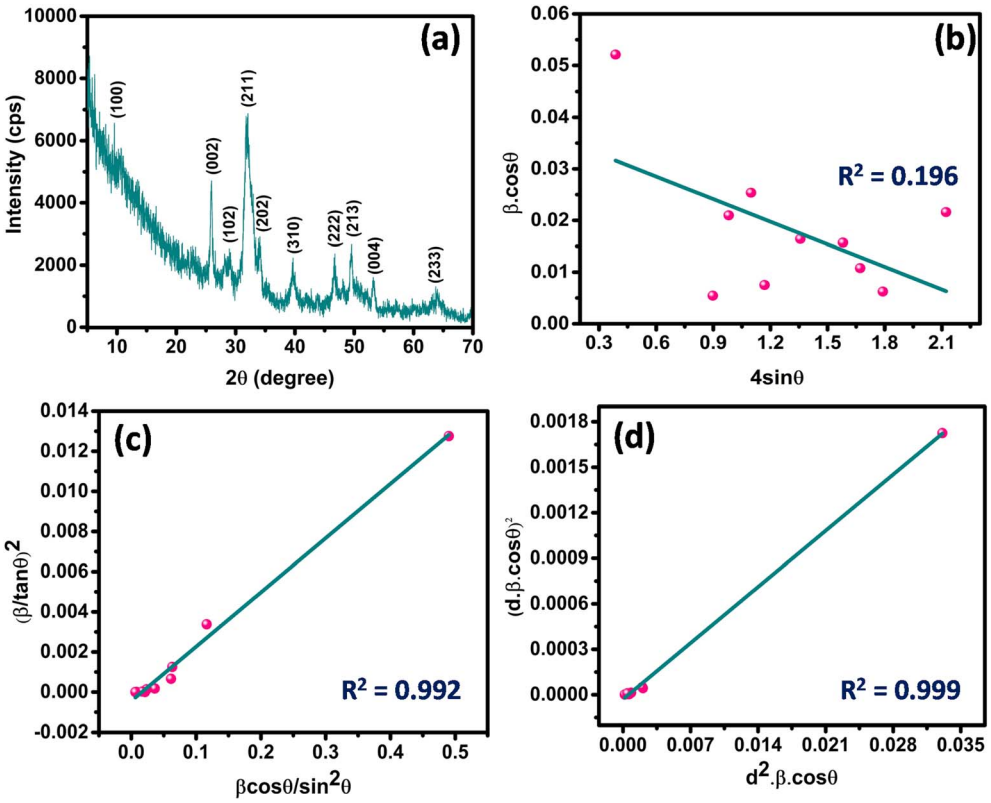

Fig. 2 (a) XRD pattern of the synthesized nHAp from micro-mollusks, (b) Williamson–Hall method (W–HM), (c) Halder–Wagner method (H–WM), and size-strain plot method (SSPM) for calculating the crystallite size.

Avogadro number (6.023×10^{23} mol^{-1}). Scherrer equation for crystallite size (D) measurement is shown in eqn (5) where k = constant (form factor, taken as 0.9), λ = wavelength of X-ray (0.154060 nm), β = full width at half maxima (FWHM) of (211) plane, and θ = diffraction angle. Micro-strain (ε) and dislocation density are presented by eqn (6) and (7) respectively. Degree of crystallinity (X_c) is presented by eqn (8) where K_a = 0.24, which is a constant.[21]

In addition to Scherrer's method for calculating the crystallite size, five other methods were also employed: Scherrer equation average method (SEAM), Straight line passing through origin method (SLPOM) (eqn (9)), Williamson–Hall method (W–HM) (eqn (10)), Halder–Wagner method (H–WM) (eqn (11)), and size-strain plot method (SSPM) (eqn (12)).[9,27,28]

$$\text{Slope} = \frac{x_1y_1 + x_2y_2 + x_3y_3 + \ldots + x_ny_n}{x_1^2 + x_2^2 + x_3^2 + \ldots + x_n^2} \quad (9)$$

$$\beta \cos\theta = \frac{K\lambda}{D} + 4\varepsilon \sin\theta \quad (10)$$

$$\left(\frac{\beta}{\tan\theta}\right)^2 = \frac{K\lambda}{D} \times \frac{\beta \cos\theta}{\sin^2\theta} + 16\varepsilon^2 \quad (11)$$

$$(d\beta \cos\theta)^2 = \frac{K\lambda}{D} \times (d^2\beta \cos\theta) + \frac{\varepsilon^2}{4} \quad (12)$$

The SEAM simply employs the FWHM of all the selected peaks in Scherrer equation to calculate the crystallite size and then makes an average. On the other hand, SLPOM considers linear fitting the plot of cos θ *versus* $1/\beta$ to pass through the origin. Here, values of $1/\beta$ are considered as x and values of cos θ are considered as y. These values are then inserted to eqn (9) to calculate the slope which is equal to $K\lambda/D$. From this relationship, value of D is calculated. For the W–HM, H–WM and SSPM, linear fitted plots of $\beta \cos\theta$ *vs.* 4 sin θ, $(\beta/\tan\theta)^2$ *vs.* ($\beta \cos\theta/\sin^2\theta$) and $(d\beta \cos\theta)^2$ *vs.* $d^2\beta \cos\theta$ are created respectively (Fig. 2b–d). The slope of these plots also equals to $K\lambda/D$, from which the crystallite size can be calculated. The crystallographic parameters of the synthesized nHAp from micro-mollusks are presented in Table 2.

3.2. FTIR analysis

In order to determine the functional groups, present in the nHAp sample, FTIR spectrum was recorded (Fig. 3). A sharp absorption peak at 3570 cm^{-1} indicates the presence of OH$^-$ functional group.[29] The broad band observed at 1020 cm^{-1} can be assigned to PO_4^{3-} asymmetric stretching vibration mode. Observed absorption peaks at 960 cm^{-1}, 560 cm^{-1}, and 440 cm^{-1} can be assigned to PO_4^{3-} symmetric stretching and bending vibration mode, respectively.[30] In addition, bending mode of water (H_2O) molecules showed a broad absorption peak at 1650 cm^{-1} which might be due to the formation of

Table 2 Crystallographic parameters of micro-mollusk derived nHAp based on the XRD data

Parameters		nHAp	ICDD file #96-900-2215
Unit cell dimensions (Å)		$a = b = 9.4935$	$a = b = 9.4390$
		$c = 6.866$	$c = 6.8860$
Volume of unit cell, V (Å^3)		535.91	531.31
Density of unit cell, ρ (g cm^{-3})		3.11	3.14
Micro-strain, ε		1.62	—
Dislocation density, δ (nm^{-2}) $\times 10^{-3}$		0.94	—
Crystallinity index (CI = X_c)		0.00268	—
Crystallite size (nm)	Scherrer equation	5.46	—
	Scherrer equation average method (SEAM)	11.74	—
	Straight line passing through origin method (SLPOM)	16.46	—
	Williamson–Hall method (W–HM)	3.72 ($R^2 = 0.196$)	—
	Halder–Wagner method (H–WM)	5.13 ($R^2 = 0.992$)	—
	Size-strain plot method (SSPM)	2.62 ($R^2 = 0.999$)	—

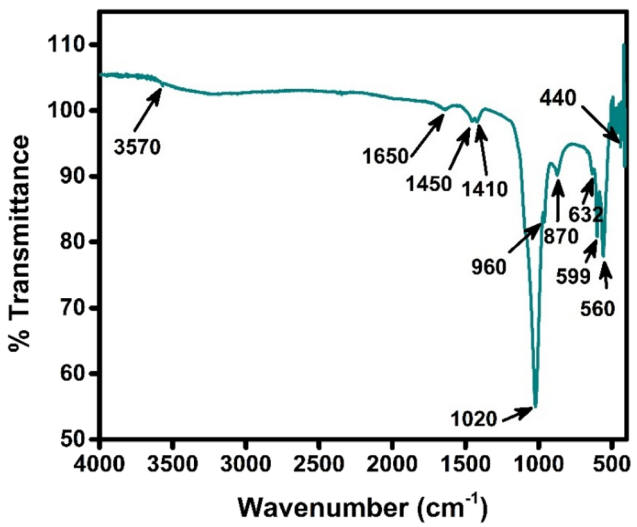

Fig. 3 FTIR spectrum with marked peak positions of the synthesized nHAp from micro-mollusks.

hydrated apatite.[30] Additionally, two absorption peaks at 1410 cm^{-1}, 1450 cm^{-1} and a band at 870 cm^{-1} confirms the presence of CO_3^{2-} in the synthesized hydroxyapatite lattice. These absorption peak values suggests the formation of B-type CO_3^{2-} substitution in HAp lattice.[31,32] All the assigned peaks are summarized in Table 3.

Table 3 FTIR spectrum data observation and peak assignments

Wavenumber (cm^{-1})	Peak assignment
3570	Hydroxyl stretching (–OH)
1650	O–H–O bending mode
1410	CO_3^{2-} asymmetric stretching
1450	CO_3^{2-} asymmetric stretching
1020	PO_4^{3-} asymmetric stretching
960	PO_4^{3-} symmetric stretching
870	CO_3^{2-} out-of-plane bending
630	PO_4^{3-} bending
560	PO_4^{3-} bending
440	PO_4^{3-} out-of-plane bending

3.3. Raman spectroscopic analysis

In addition to FTIR, Raman spectroscopy was also utilized to detect vibrational modes, and to acquire information about the molecular structure and phase purity of the synthesized nHAp sample. Fig. 4 shows the Raman spectrum of the synthesized nHAp. The distinct peaks observed at 434 cm^{-1}, 588 cm^{-1}, 966 cm^{-1}, and 1052 cm^{-1} corresponds to the tetrahedral PO_4^{3-} group vibrational mode of symmetrical bending (υ_2), asymmetric bending (υ_4), symmetric stretching (υ_1), and symmetric stretching (υ_3), respectively.[23]

When carbonate groups (typically as B-type substitution where CO_3^{2-} replaces PO_4^{3-}) are present in HAp, the most characteristic and commonly observed Raman peak for the carbonate is the symmetric stretching mode (υ_1 CO_3^{2-}) at approximately 1070 cm^{-1}. However, this peak often overlaps with the υ_1 PO_4^{3-} mode of phosphate, leading to a composite band in the 1000–1100 cm^{-1} region whose shape and intensity vary with carbonate content.[33]

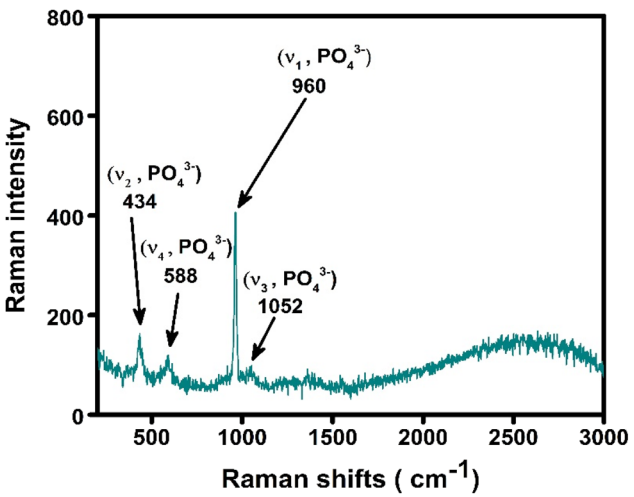

Fig. 4 Raman spectrum of micro-mollusk-derived nHAp.

3.4. FESEM and EDX analysis

The surface morphology of synthesized nHAp was analyzed using FESEM. Fig. 5a and b shows the FESEM images at two different magnifications and Fig. 5b particularly shows the particle boundary selections for size measurements. The images show that the particles of nHAp exist with both agglomerates and aggregates, and is evident to have elongated and distorted oval shapes.[23] The average particle size was found to be 32.11 ± 11.38 nm by measuring the size of 105 particles using ImageJ software and the size distribution histogram is presented in Fig. 5c (ImageJ software was used by following the procedure reported in our previous literature[27]). This indicates a narrow size distribution that increases the materials ability to be used for various applications such as bone regeneration, drug delivery due to high surface area and availability of more active sites.[34] Furthermore, EDX spectroscopy was utilized for elemental analysis of the sample. The EDX spectra (Fig. 5d) shows peak for Ca, P, and O which confirms the presence of primary elements required to form HAp. The additional peak for C may be due to the existing carbonate group as found from the FTIR spectrum or the atmospheric contamination or the carbon tape substrate required to hold the sample.[9] Additionally, the atom% of Ca and P was 14.70% and 12.49% respectively, and the calculated Ca/P ratio is 1.17, which is lower than the stoichiometric ratio of 1.67 found in standard HAp. This indicates the formation of Ca-deficient HAp.[24,35] The variation in this value can be attributed to the low-level carbonate substitution as confirmed by FTIR analysis. Elemental mapping images of the sample (Fig. 5e) show distinct elemental distribution pattern of the sample. From the images, it can be seen that Calcium (Ca K), Phosphorus (P K), and Oxygen (O K) strongly correlates which indicates the formation of a relatively homogenous phase. On the other hand, C has a more limited distribution that further indicates the presence of carbon.[20] Quantitative result of EDX has been presented in Fig. 5f.

3.5. TEM analysis

TEM analysis of the synthesized nHAp sample is shown in Fig. 6. The two TEM images at two different magnifications (Fig. 6a and b) confirm the elongated and distorted oval shaped particles with major agglomeration and aggregation as seen in FESEM images. The average particle size was measured to be 14.95 ± 5.37 nm ($N = 33$) (Fig. 6c). Furthermore, Fig. 6d presents high resolution image that clearly shows lattice fringes and depicts the existence of crystalline nature in the synthesized sample. In addition, the characteristic pattern of a polycrystalline material is evident from the SAED pattern (Fig. 6e), which consists of sharp concentric rings with distinct diffraction spots.

3.6. Surface chemistry analysis by XPS

The XPS survey spectrum is presented in Fig. 7a where binding energies were referenced to adventitious C 1s at 284.8 eV. The survey spectrum revealed distinct peaks which correspond to Ca, P, O and C that belongs to the elemental composition of HAp.[36] Strong peaks of Ca 2p, P 2p and O 1s can be observed from the spectra is indicative of a calcium phosphate phase,

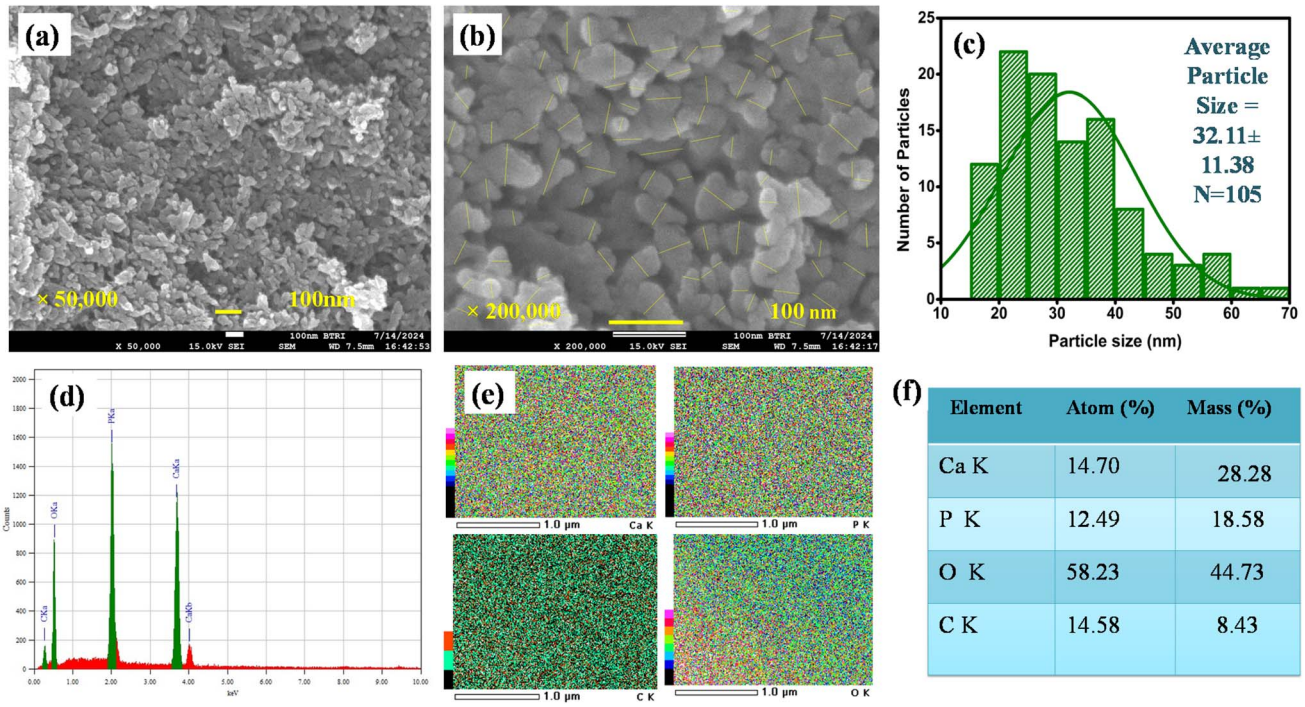

Element	Atom (%)	Mass (%)
Ca K	14.70	28.28
P K	12.49	18.58
O K	58.23	44.73
C K	14.58	8.43

Fig. 5 (a) and (b) FESEM images at two different magnifications, as well as particle selection for size measurements, (c) particle size distribution histogram, (d) EDX spectra, (e) elemental mapping of the detected elements, and (f) atom% and mass% of the elements present in the micro-mollusk derived nHAp sample.

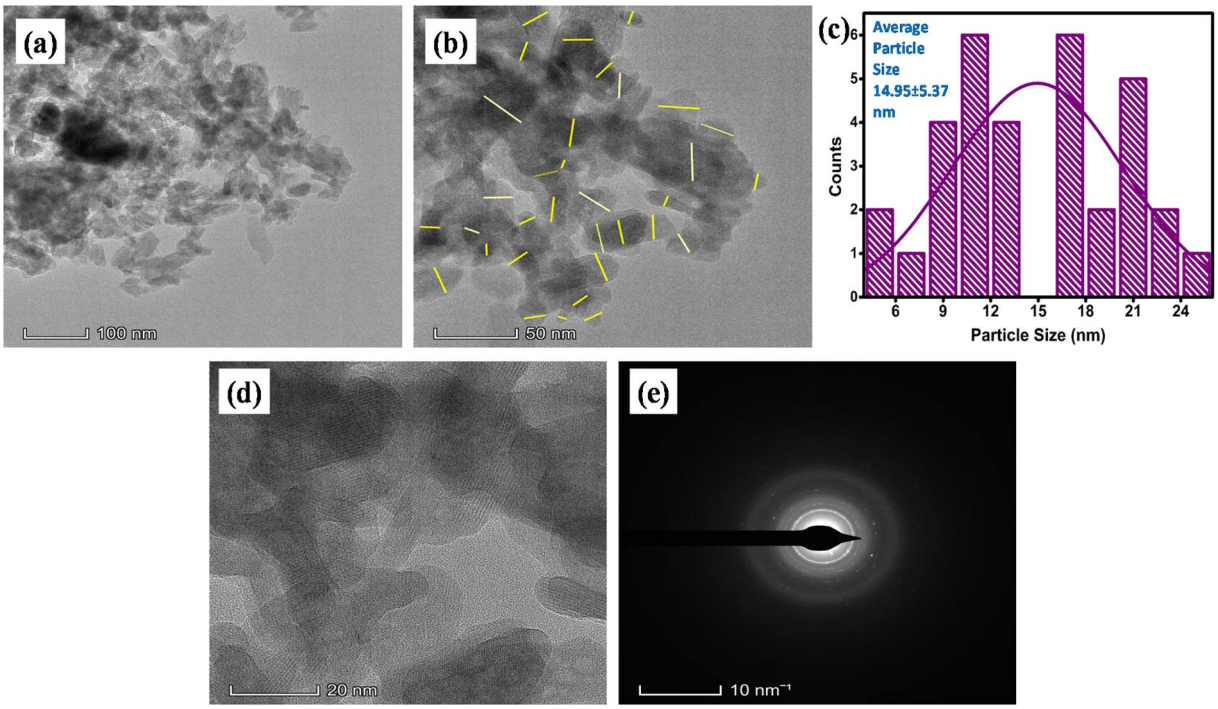

Fig. 6 (a) and (b) TEM images at two different magnifications, as well as particle selection for size measurements, (c) particle size distribution histogram, (d) high resolution image showing lattice fringes, and (e) SAED pattern showing polycrystalline nature of the synthesized nHAp.

while C 1s signal arises mainly from surface carbon contamination (also termed as adventitious carbon) or the present carbonate content confirmed through the FTIR and Raman spectroscopic analysis. Presence of Na (0.27 atom%) was also detected. Similar XPS survey spectra and profile was observed in our previous studies where HAp was synthesized from *Conus litteratus* seashells.[8,37]

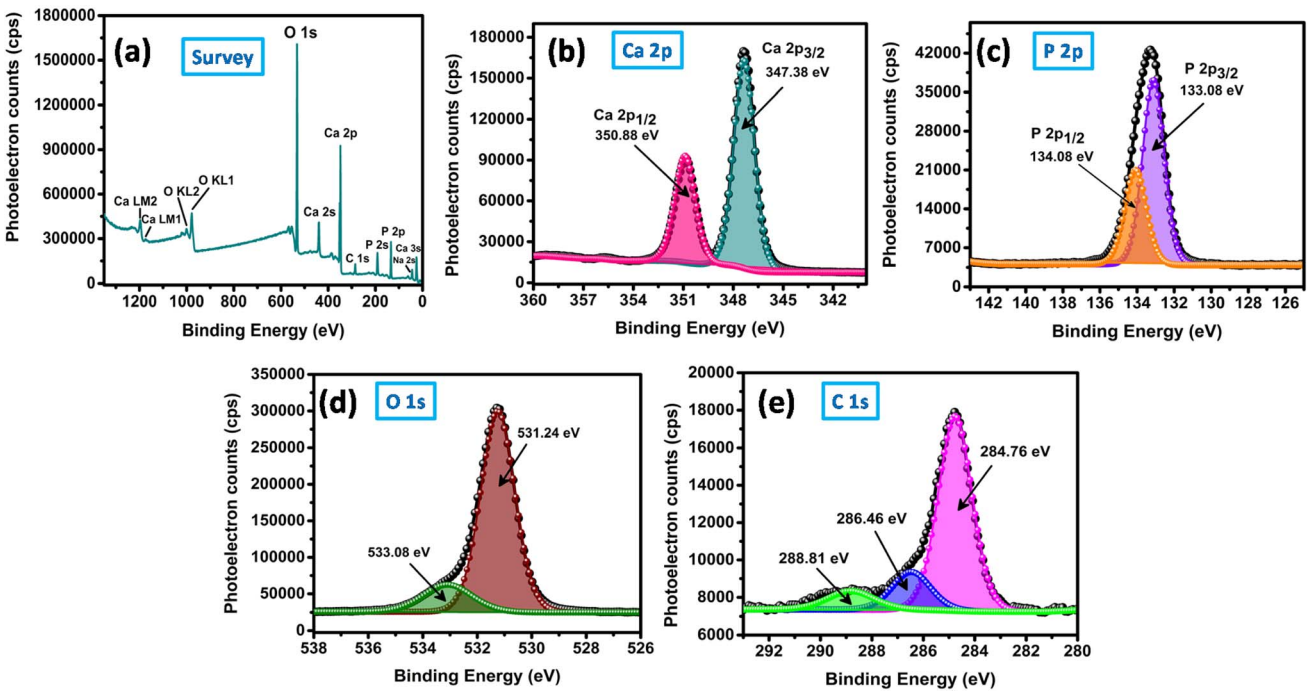

Fig. 7 XPS spectra of micro-mollusk-derived nHAp: (a) survey scan showing Ca, P, O, and C peaks; (b) Ca 2p, (c) P 2p, (d) O 1s, and (e) C 1s core-level spectra with deconvoluted components.

The Ca 2p spectrum (Fig. 7b) shows two well-resolved peaks at 347.38 eV (Ca $2p_{3/2}$) and 350.88 eV (Ca $2p_{1/2}$) that are characteristic of Ca^{2+} in HAp lattices.[38] Deconvolution of P 2p signal (Fig. 7c) resulted in two distinct peaks. The P 2p doublet at 133.08 eV (P $2p_{3/2}$) and 134.08 eV (P $2p_{1/2}$) corresponds to the phosphate group (PO_4^{3-}), also consistent with the stoichiometric HAp.[39] The O 1s spectrum (Fig. 7d) displays two components upon deconvolution; a dominant peak at 531.24 eV attributed to O in phosphate (P–O) bonds and a minor peak at 533.08 eV due to surface hydroxyl or adsorbed water species.[25] The C 1s spectrum (Fig. 7e) includes peaks at 284.76 eV, 286.46 eV, and 288.81 eV, which correspond to C–C/C–H, C–O, and CO_3^{2-} binding, respectively. This also suggests presence of minor carbonate contamination, which is common for seashell-derived calcium phosphates exposed to atmospheric CO_2.

3.7. TGA and DSC analysis

The thermal behavior of micro-mollusk-derived nHAp was investigated using a simultaneous thermal analyzer (STA) under a nitrogen atmosphere at a heating rate of 2.7 K min^{-1} from ambient temperature to 600 °C. The TG curve (Fig. 8a) exhibited a total mass loss of approximately 7.7%, with a residual mass of 92.2% at 597.5 °C. The initial minor weight decrease (0.39%) observed below 50 °C corresponds to the release of physically adsorbed moisture from the nHAp surface. A subsequent weight loss of 2.2% in the temperature range of 50–150 °C is attributed to the removal of structural water and loosely bound hydroxyl groups. The third and fourth mass changes of 1.14% and 2.78%, respectively, between 150 and 350 °C can be ascribed to the decomposition of organic residues originating from the seashell matrix and partial dehydroxylation of the HAp lattice. Beyond 350 °C, minor mass reductions of 0.33, 0.55 and 1.01% were observed, which may indicate carbonate decomposition or the elimination of residual biogenic components.[40–42]

The DSC thermogram (Fig. 8b) revealed an endothermic feature below 150 °C corresponding to moisture evaporation, followed by a nearly steady exothermic trend up to 600 °C. The gradual exothermic rise suggests structural reorganization and improved crystallinity of the HAp phase upon heating. The absence of sharp endothermic or exothermic peaks above 400 °C confirms the thermal stability of the synthesized nHAp, consistent with the minimal weight loss observed in the TG curve. Overall, the TG-DSC results confirm that the micro-mollusk-derived nHAp exhibits excellent thermal stability up to 600 °C, with only minor mass losses related to dehydration and the decomposition of residual organic or carbonate species.

3.8. BET surface area analysis

The textural characteristics of the micro-mollusk-derived nHAp sample were determined through N_2 adsorption–desorption measurements at 77 K, and the corresponding isotherm and pore size distribution curves are presented in Fig. 9. The nitrogen adsorption–desorption isotherm displays a type IV profile with a H3-type hysteresis loop, as per the IUPAC classification, confirming the mesoporous nature of the synthesized HAp.[43]

At low relative pressures ($P/P_0 < 0.2$), a gradual increase in adsorbed volume is observed, indicating monolayer adsorption of nitrogen molecules on the nHAp surface. This region reflects the adsorption on the external surface and within micropores, where the interaction between nitrogen molecules and the surface dominates over intermolecular forces.[44] As the relative pressure increases to the intermediate region ($0.2 < P/P_0 < 0.8$), the adsorption volume increases steadily, suggesting the progressive formation of multilayers on the pore walls and the onset of capillary condensation within mesopores.[8] This behavior is typical of mesoporous solids with uniform pore geometry.

A pronounced hysteresis loop appears in the high-pressure range (P/P_0 = 0.8–1.0), corresponding to capillary condensation and evaporation occurring within interconnected mesopores and slit-shaped voids.[45] The hysteresis loop is of the H3 type, which is generally associated with aggregates of plate-like particles forming slit-shaped pores,[46] consistent with the morphology of HAp derived from biogenic Ca sources.[47] The BET plot (inset of Fig. 9a) exhibits excellent linearity in the relative pressure range of 0.05–0.30 with a correlation coefficient of R^2 = 0.9999, validating the applicability of the BET model. From this linear region, the specific surface area was calculated to be 72.98 m^2 g^{-1}, while the total pore volume and

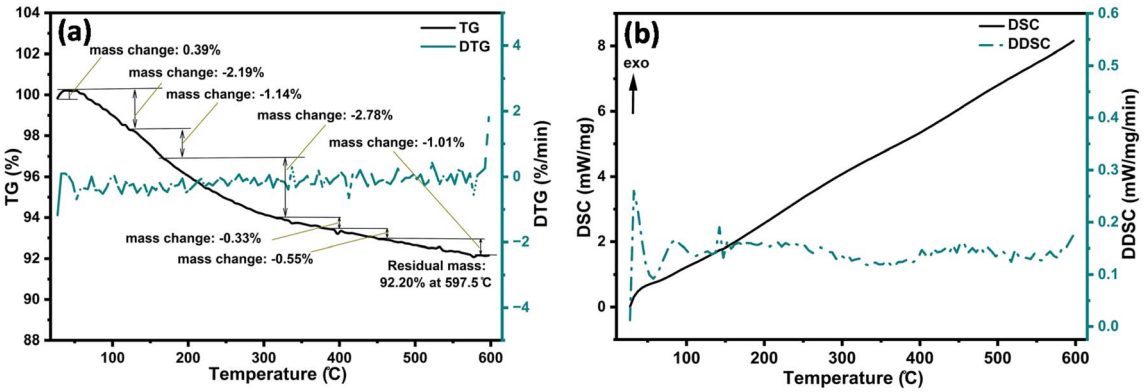

Fig. 8 Simultaneous thermal analysis of micro-mollusk derived nHAp: (a) TGA-DTG plots and (b) DSC-DDSC plots.

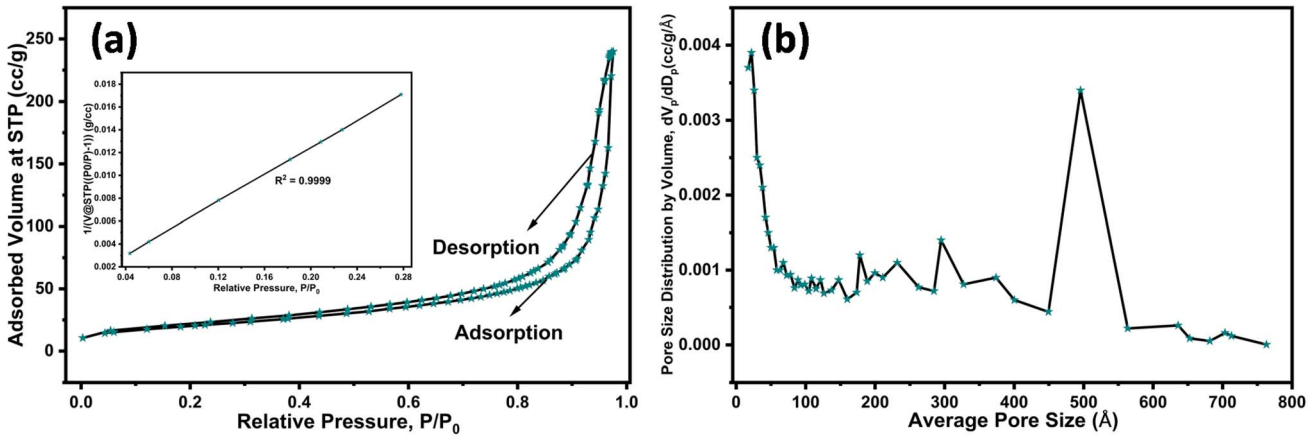

Fig. 9 (a) N_2 adsorption–desorption isotherm, (b) BJH adsorption pore size distribution curve of the synthesized nHAp sample.

average pore diameter were found to be 0.3694 $cm^3\ g^{-1}$ and 202.45 Å (20.24 nm), respectively. The BJH pore size distribution curve (Fig. 9b) confirms the presence of mesopores with a dominant pore size in the range of 200–500 Å (20–50 nm), and a sharp peak centered around ~500 Å (50 nm), indicating a moderately broad pore size distribution. The coexistence of mesopores and macropores is indicative of hierarchical porosity beneficial for diffusion-controlled applications.[48]

3.9 Cell viability study

The cytocompatibility or cell viability of the synthesized nHAp sample was evaluated using Vero cell lines after 24 hours of incubation. Fig. 10a–c shows the optical microscopy images of cells treated with nHAp, positive control, and negative control, respectively. The cells in all groups exhibited normal morphology with well-defined cell boundaries, uniform spreading, and no noticeable signs of deformation or detachment. The dark spots observed in the optical micrographs correspond to minor cell debris or minor particulate or imaging artifacts, which are commonly observed in optical microscopy of cultured cells. They are also present in the control groups, indicating that they are not related to cytotoxic effects. The cell viability result (Table 4) indicated that more than 95% of the Vero cells remained viable after exposure to the nHAp sample at a concentration of 100 μg mL^{-1}. This value is comparable to the positive control and only slightly lower than the untreated negative control, which showed 100% viability. The absence of morphological abnormalities and high survival rate confirm that the synthesized nHAp sample is non-toxic and supports normal cell proliferation.[25]

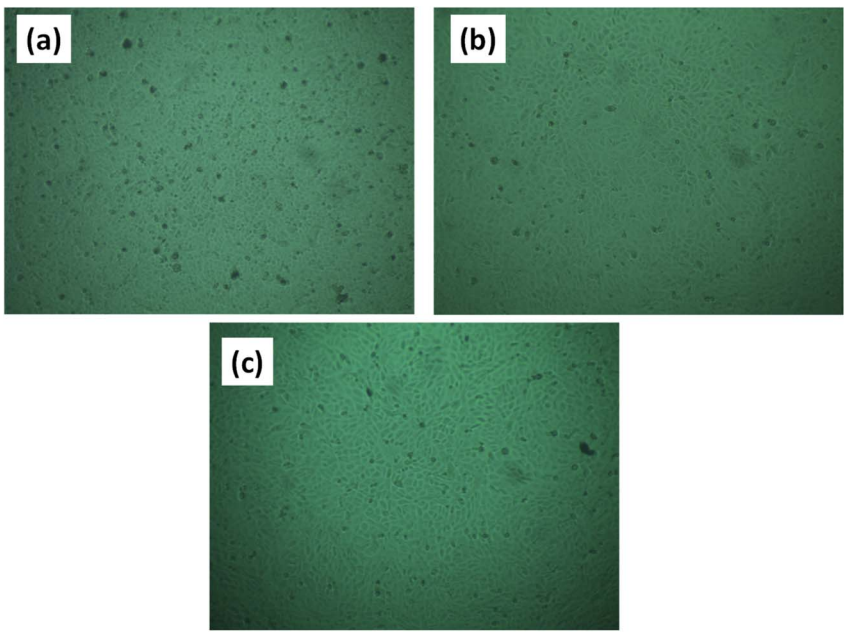

Fig. 10 Optical microscopy images of Vero cells cultured with (a) nHAp (b) positive control (DMEM), (c) negative control (PBS).

Table 4 Results of cell viability assay (sample amount 25 μL each and incubation period 24 h)

Sample name	Sample concentration	Cell viability	Result
nHAp	100 μg mL^{-1}	>95%	The sample shows no signs of cytotoxicity
Solvent +	—	>95%	
Solvent −	—	100%	

4. Conclusion

In this study, successful synthesis of nHAp was achieved by utilizing a seashell waste (micro-mollusks) *via* simple wet chemical method. Formation of HAp phase was confirmed by X-ray diffraction analysis, along with other crystallographic parameters. Existence of different functional groups of HAp was deciphered by FTIR and Raman spectroscopic analysis. The nano-size nature of the synthesized HAp particles was confirmed by FESEM and TEM image-based particle size analysis. This nano-sized nature of nHAp contributed to its large surface area as confirmed by the BET analysis. Additionally, thermal analysis (carried out up to 600 °C) revealed high thermal stability of nHAp. The surface elemental composition was analyzed by XPS while the bulk elemental composition was analyzed by EDX. Compared with the WDXRF result of the micro-mollusk, XPS and EDX analysis of nHAp have confirmed the elimination of most of the element in the final product. This is also an indication of product purity and effectiveness of our adopted synthesis route. The cell viability study indicates that the prepared nHAp is one of the safest materials with superior biocompatibility and have the potential to be used in biomedical applications.

Author contributions

Mashrafi Bin Mobarak: conceptualization, investigation, supervision, funding acquisition, project administration, writing – original draft, writing – review & editing; Md Sohag Hossain: methodology, investigation, data curation, writing – original draft; Aima Tanjim Khan – data curation, writing – original draft; Fariha Chowdhury: formal analysis, investigation, data curation, writing – original draft; Samina Ahmed: supervision, resources.

Conflicts of interest

There is no conflict to declare.

Data availability

All data of this study are included in the manuscript. Raw data will be available from the corresponding author upon reasonable request.

Acknowledgements

This research work was supported by Bangladesh Council of Scientific and Industrial Research (BCSIR) through R&D project (ref. no. 39.02.0000.011.14.200.2025.1326; Date: 16.11.2025). We would like to extend our heartfelt gratitude to: Juliya Khanam, Monira Binte Mesbah, Nazmul Islam Tanvir, Umme Sarmeen Akhtar, Md. Saiful Quddus, Md. Farid Ahmed, and Sharuk Alam Aumi for helping out with the WDXRF, XRD, Raman, XPS, BET, STA and Cytotoxicity analysis, respectively.

References

1 R.-M. Kavasi, C. C. Coelho, V. Platania, P. A. Quadros and M. Chatzinikolaidou, *Nanomaterials*, 2021, **11**, 1152.
2 E. Fiume, G. Magnaterra, A. Rahdar, E. Verné and F. Baino, *Ceramics*, 2021, **4**, 542–563.
3 M. B. Mobarak, M. S. Hossain, Z. Yeasmin, M. Mahmud, M. M. Rahman, S. Sultana, S. M. Masum and S. Ahmed, *J. Mol. Struct.*, 2022, **1252**, 132142.
4 L. C. Palmer, C. J. Newcomb, S. R. Kaltz, E. D. Spoerke and S. I. Stupp, *Chem. Rev.*, 2008, **108**, 4754–4783.
5 E. Pepla, L. K. Besharat, G. Palaia, G. Tenore and G. Migliau, *Ann. Stomatol.*, 2014, **5**, 108–114.
6 V. G. DileepKumar, M. S. Sridhar, P. Aramwit, V. K. Krut'ko, O. N. Musskaya, I. E. Glazov and N. Reddy, *J. Biomater. Sci., Polym. Ed.*, 2022, **33**, 229–261.
7 P. Arokiasamy, M. M. Al Bakri Abdullah, S. Z. Abd Rahim, S. Luhar, A. V. Sandu, N. H. Jamil and M. Nabiałek, *Ceram. Int.*, 2022, **48**, 14959–14979.
8 M. S. Hossain, M. S. Hossain, S. Ahmed and M. B. Mobarak, *RSC Adv.*, 2024, **14**, 38560–38577.
9 M. B. Mobarak, M. N. Uddin, F. Chowdhury, M. S. Hossain, M. Mahmud, S. Sarkar, N. I. Tanvir and S. Ahmed, *J. Mol. Struct.*, 2024, **1301**, 137321.
10 P. C. Okpe, O. Folorunso, V. S. Aigbodion and C. Obayi, *J. Biomed. Mater. Res., Part B*, 2024, **112**, e35440.
11 M. C. Barros, P. M. Bello, M. Bao and J. J. Torrado, *J. Cleaner Prod.*, 2009, **17**, 400–407.
12 K. S. Vecchio, X. Zhang, J. B. Massie, M. Wang and C. W. Kim, *Acta Biomater.*, 2007, **3**, 910–918.
13 S. Hussain and K. Sabiruddin, *Ceram. Int.*, 2021, **47**, 29660–29669.
14 S. H. Saharudin, J. H. Shariffuddin, A. Ismail and J. H. Mah, *Bull. Mater. Sci.*, 2018, **41**, 162.
15 M. Harkat, S. Alleg, R. Chemam, N. Moutia, K. Khirouni and E. Dhahri, *Arabian J. Sci. Eng.*, 2022, **47**, 7693–7706.
16 K. M. Kocot, F. Aguilera, C. McDougall, D. J. Jackson and B. M. Degnan, *Front. Zool.*, 2016, **13**, 23.
17 N. Topić Popović, V. Lorencin, I. Strunjak-Perović and R. Čož-Rakovac, *Appl. Sci.*, 2023, **13**, 623.
18 J. Leal, *The Allure of Small Size*, https://shellmuseum.org/blog/the-allure-of-small-size/, accessed November 5, 2025.

19 L. Qi, B. Xu, L. Kong and Q. Li, *Biodiversity Data J.*, 2023, **11**, e105444.
20 M. B. Mobarak, S. A. Fahim, M. S. Hossain, F. Chowdhury, N. I. Tanvir, U. S. Akhtar and S. Ahmed, *ACS Sustainable Resour. Manage.*, 2025, **2**, 1528–1539.
21 M. Bin Mobarak, S. Tabassum, M. Sohag Hossain, N. Tarannum, F. Chowdhury, M. S. Hossain, N. Islam Tanvir and S. Ahmed, *RSC Adv.*, 2025, **15**, 35617–35633.
22 R. M. Wilson, J. C. Elliott and S. E. P. Dowker, *Am. Mineral.*, 1999, **84**, 1406–1414.
23 M. B. Mobarak, M. N. Islam, F. Chowdhury, M. N. Uddin, M. S. Hossain, M. Mahmud, U. S. Akhtar, N. I. Tanvir, A. M. Rahman and S. Ahmed, *RSC Adv.*, 2023, **13**, 36209–36222.
24 M. B. Mobarak, F. Chowdhury, M. N. Uddin, M. S. Hossain, U. Akhtar, N. I. Tanvir, M. A. A. Shaikh and S. Ahmed, *Mater. Adv.*, 2024, **5**, 9716–9730.
25 M. B. Mobarak, F. Chowdhury and S. Ahmed, *RSC Adv.*, 2024, **14**, 39874–39889.
26 M. B. Mobarak, M. S. Hossain, F. Chowdhury, N. Tarannum, M. B. Mesbah, N. I. Tanvir, U. S. Akhtar and S. Ahmed, *RSC Adv.*, 2025, **15**, 38454–38469.
27 M. Bin Mobarak, Md. S. Hossain, F. Chowdhury and S. Ahmed, *Arabian J. Chem.*, 2022, **15**, 104117.
28 F. Chowdhury, M. B. Mobarak, M. Hakim, M. N. Uddin, M. S. Hossain, U. S. Akhter, D. Islam, S. Ahmed and H. Das, *New J. Chem.*, 2024, **48**, 17038–17051.
29 I. Rehman and W. Bonfield, *J. Mater. Sci.:Mater. Med.*, 1997, **8**, 1–4.
30 S. Sultana, M. S. Hossain, M. Mahmud, M. B. Mobarak, M. H. Kabir, N. Sharmin and S. Ahmed, *RSC Adv.*, 2021, **11**, 3686–3694.
31 M. M. Ariffin, N. I. Yatim and S. Hamzah, *Malays. J. Anal. Sci.*, 2017, **21**(3), 571–584.
32 J. C. Merry, I. R. Gibson, S. M. Best and W. Bonfield, *J. Mater. Sci.:Mater. Med.*, 1998, **9**, 779–783.
33 A. Awonusi, M. D. Morris and M. M. J. Tecklenburg, *Calcif. Tissue Int.*, 2007, **81**, 46–52.
34 J. W. Hickey, J. L. Santos, J.-M. Williford and H.-Q. Mao, *J. Controlled Release*, 2015, **219**, 536–547.
35 J. O. Akindoyo, S. Ghazali, M. D. H. Beg and N. Jeyaratnam, *Chem. Eng. Technol.*, 2019, **42**, 1805–1815.
36 M. B. Mobarak, N. S. Pinky, F. Chowdhury, M. S. Hossain, M. Mahmud, M. S. Quddus, S. A. Jahan and S. Ahmed, *J. Saudi Chem. Soc.*, 2023, 101690.
37 M. S. Hossain, Md. Sahadat Hossain, F. Chowdhury, Md. S. Quddus, U. S. Akhtar, N. I. Tanvir, S. Ahmed and M. B. Mobarak, *ACS Sustainable Resour. Manage.*, 2025, **2**(10), 1917–1928.
38 V. Uskoković, *Phys. Chem. Chem. Phys.*, 2020, **22**, 5531–5547.
39 G. C. Gomes, F. F. Borghi, R. O. Ospina, E. O. López, F. O. Borges and A. Mello, *Surf. Coat. Technol.*, 2017, **329**, 174–183.
40 N. Böhme, K. Hauke, M. Dohrn, M. Neuroth and T. Geisler, *J. Mater. Sci.*, 2022, **57**, 15239–15266.
41 H. Lian, X. Liu and Z. Meng, *J. Mater. Sci.*, 2019, **54**, 719–729.
42 N. V. Bulina, S. V. Makarova, S. G. Baev, A. A. Matvienko, K. B. Gerasimov, O. A. Logutenko and V. S. Bystrov, *Minerals*, 2021, **11**, 1310.
43 M. M. Rahman, M. Muttakin, A. Pal, A. Z. Shafiullah and B. B. Saha, *Energies*, 2019, **12**, 4565.
44 A. Medjdoub, F. Nemchi, H. Belayachi, B. Bestani, S. Bourahla, M. Belhakem and N. Benderdouche, *Desalin. Water Treat.*, 2022, **252**, 348–360.
45 J. A. Lett, S. Sagadevan, J. J. Prabhakar, N. A. Hamizi, I. A. Badruddin, M. R. Johan, A. R. Marlinda, Y. Abdul Wahab, T. M. Yunus Khan and S. Kamangar, *Processes*, 2019, **7**, 826.
46 Y. Xie, J. Xie, L. Bai, J. Wang and J. Liu, *Constr. Build. Mater.*, 2025, **495**, 143221.
47 N. Safitri, N. Rauf and D. Tahir, *Polym. Bull.*, 2025, **82**, 10639–10670.
48 H. Lv, N. Li, J. Zhang, Y. Hou, X. Fan, X. Liu and F. Dang, *Small*, 2025, **21**, 2411525.